

XL-Calibur polarimetry of Cyg X-1 further constrains the origin of its hard-state X-ray emission

HISAMITSU AWAKI,¹ MATTHEW G. BARING,² RICHARD BOSE,³ JACOB CASEY,⁴ SOHEE CHUN,³ ADRIKA DASGUPTA,⁴
PAVEL GALCHENKO,⁵ EPHRAIM GAU*,³ KAZUHO GOYA,⁶ TOMOHIRO HAKAMATA,⁷ TAKAYUKI HAYASHI,^{8,9}
SCOTT HEATWOLE,⁵ KUN HU**,³ DAIKI ISHI,¹⁰ MANABU ISHIDA,¹⁰ FABIAN KISLAT,⁴ MÓZSI KISS†,^{11,12} KASSI KLEPPER,^{11,12}
HENRIC KRAWCZYNSKI,³ HARUKI KURAMOTO,⁷ LINDSEY LISALDA,³ YOSHITOMO MAEDA,¹⁰ HIRONORI MATSUMOTO,^{7,13}
SHRAVAN VENGALIL MENON,³ AIKO MIYAMOTO,⁷ ASCA MIYAMOTO,¹⁴ KAITO MURAKAMI,⁷ TAKASHI OKAJIMA,⁸
MARK PEARCE,^{11,12} BRIAN RAUCH,³ NICOLE RODRIGUEZ CAVERO,³ KENTARO SHIRAHAMA,⁷ SEAN SPOONER‡,⁴
HIROMITSU TAKAHASHI,⁶ KEISUKE TAMURA,^{8,9} YUUSUKE UCHIDA,¹⁵ KASUN WIMALASENA,⁴ MASATO YOKOTA,⁶ AND
MARINA YOSHIMOTO⁷

¹Graduate School of Science and Engineering, 2-5, Bunkyo-cho, Matsuyama, Ehime 790-8577, Japan

²Department of Physics and Astronomy – MS 108, Rice University, 6100 Main Street, Houston, Texas 77251-1892, USA

³Department of Physics, McDonnell Center for the Space Sciences and Center for Quantum Sensors, Washington University in St. Louis, 1 Brookings Dr, Saint Louis, MO 63130, USA

⁴Department of Physics and Astronomy, and Space Science Center, University of New Hampshire, 8 College Rd, Durham, NH 03824, USA

⁵NASA Wallops Flight Facility, Fulton St, Wallops Island, VA 23337, USA

⁶Graduate School of Advanced Science and Engineering, Hiroshima University, 1-3-1 Kagamiyama, Higashi-Hiroshima, Hiroshima 739-8526, Japan

⁷Department of Earth and Space Science, Osaka University, 1-1 Machikaneyama-cho, Toyonaka, Osaka 560-0043, Japan

⁸NASA Goddard Space Flight Center, Greenbelt, MD 20771, USA

⁹University of Maryland, Baltimore County, 1000 Hilltop Circle, Baltimore, MD 21250, USA

¹⁰Japan Aerospace Exploration Agency, Institute of Space and Astronautical Science, 3-1-1 Yoshino-dai, Chuo-ku, Sagami-hara, Kanagawa 252-5210, Japan

¹¹KTH Royal Institute of Technology, Department of Physics, 106 91 Stockholm, Sweden

¹²The Oskar Klein Centre for Cosmoparticle Physics, AlbaNova University Center, 106 91 Stockholm, Sweden

¹³Forefront Research Center, Graduate School of Science, Osaka University, Japan

¹⁴Department of Physics, Tokyo Metropolitan University, 1-1 Minami-Osawa, Hachioji, Tokyo 192-0397, Japan

¹⁵Tokyo University of Science, 2641 Yamazaki, Noda, Chiba 278-8510, Japan

ABSTRACT

The balloon-borne hard X-ray polarimetry mission *XL-Calibur* observed the Black Hole X-ray Binary (BHXR) Cygnus X-1 (Cyg X-1) during its nearly six-day Long Duration Balloon (LDB) flight from Sweden to Canada in July 2024. The *XL-Calibur* observations allowed us to derive the most precise constraints to date of the Polarization Degree (PD) and Polarization Angle (PA) of the hard X-ray emission from a BHXR. *XL-Calibur* observed Cyg X-1 in the hard state and measured a $\sim 19\text{--}64\text{ keV}$ PD of $(5.0^{+2.7}_{-3.0})\%$ at a PA of $-28^\circ \pm 17^\circ$, with an 8.7% chance probability of detecting larger PDs than the one observed, given an unpolarized signal. The *XL-Calibur* results are thus comparable to the 2–8 keV PD and PA found by *IXPE*, with a similar agreement between the hard X-ray PA and the radio jet direction. We also discuss the implications of our polarization measurements in the context of models describing the origin of the broadband X-ray and γ -ray emission, to which *XL-Calibur* provides independent constraints on any proposed emission modeling.

Corresponding author: *Ephraim Gau (ephraimgau@wustl.edu)

Corresponding author: **Kun Hu (hkun@wustl.edu)

Corresponding author: †Mózi Kiss (mozsi@kth.se)

Corresponding author: ‡Sean Spooner (Sean.Spooner@unh.edu)

Keywords: (1) High Energy Astrophysics, (2) X-ray Polarization, (3) Balloon-borne Mission, (4) Stellar-mass Black Holes, (5) Black Hole X-ray Binaries, (6) Black Hole Accretion, (7) Black Hole Corona

1. INTRODUCTION

The polarization of the 2–8 keV X-ray emission from a variety of galactic and extragalactic sources, including BHXRBs, accretion-powered neutron stars, magnetars, pulsar wind nebulae, supernova remnants, and Active Galactic Nuclei (AGNs) (e.g., Krawczynski et al. 2022; Doroshenko et al. 2022; Taverna et al. 2022; Xie et al. 2022; Vink et al. 2022; Liodakis et al. 2022; Ehlert et al. 2022) has been measured by the *Imaging X-ray Polarimetry Explorer* (*IXPE*) (Weisskopf et al. 2022). Most relevant to our study, *IXPE* has observed BHXRBs in several states, as covered in the recent review papers of Caverio & *IXPE* Collaboration (2024) and Dovčiak et al. (2024).

The *soft-state* emission from BHXRBs is dominated by the diluted multi-temperature blackbody emission from a geometrically thin, optically thick accretion disk. Measurements of this emission constrain the inclination of the accretion disk and the black hole spin (that is, the angle between the black hole spin axis and the line of sight to the observer) (Li et al. 2009; Schnittman & Krolik 2009). The *hard-state* emission includes the Comptonized (upscattered) emission from the coronal plasma, as well as coronal emission reflected by the disk (Schnittman & Krolik 2010; Zhang et al. 2019; Krawczynski & Beheshtipour 2022; Poutanen et al. 2023). One such BHXRB, Cyg X-1, comprises a $(21.2^{+2.2}_{-2.3}) M_{\odot}$ black hole, along with a $(40.6^{+7.7}_{-7.1}) M_{\odot}$ companion, located at a distance of $(2.22^{+0.18}_{-0.17})$ kpc from Earth (Miller-Jones et al. 2021). It is found in the hard state about two-thirds of the time (Wilms et al. 2006; Grinberg et al. 2013).

The *IXPE* hard-state observations of Cyg X-1 revealed a 2–8 keV PD of $(4.01 \pm 0.20)\%$, surprisingly high when compared to the predictions of laterally-extended corona models (e.g., Schnittman & Krolik 2010; Krawczynski & Beheshtipour 2022), as well as a PA of $-20^{\circ}.7 \pm 1^{\circ}.4$ (with positive angles denoting directions East of Celestial North), which is aligned with the axis of its radio jet. The measurements indicated an increase of the PD with energy, going from $(3.6 \pm 0.4)\%$ to $(5.7 \pm 0.9)\%$ between 2 keV to 8 keV (Krawczynski et al. 2022). *IXPE* revealed a similar alignment of the coronal emission polarization with the radio jets of the BHXRBs Swift J1727.8–1613 (Veledina et al. 2023; Ingram et al. 2024; Wood et al. 2024) and GX 339–4 (Mastroserio et al. 2024), as well as the AGNs NGC 4151 (Johnston et al. 1982; Ulves-

tad et al. 1998; Gianolli et al. 2023, 2024) and IC 4329A (Unger et al. 1987; Ingram et al. 2023). This alignment thus seems to be a general feature of the coronal emission from accretion disks across a broad range of black hole masses (Saade et al. 2024). *IXPE* soft state observations of Cyg X-1 showed the PA still being aligned with the radio jet but with a somewhat lower 2–8 keV PD of $(1.99 \pm 0.13)\%$ (Steiner et al. 2024).

The hard state polarization results of BHXRBs from *IXPE* can be interpreted within different theoretical frameworks. In one family of models, the power-law X-rays originate within a horizontally-extended corona Comptonizing lower-energy synchrotron emission or standard/truncated accretion disk emission in a hot $T_C \sim 100$ keV plasma (e.g. Sunyaev & Titarchuk 1985; Poutanen & Vilhu 1993; Schnittman & Krolik 2010; Krawczynski & Beheshtipour 2022, and references therein). The high 2–8 keV PDs measured by *IXPE* in Krawczynski et al. (2022) could be explained by the models analyzed in that study, but only if the inner disk inclination is $\geq 45^{\circ}$, substantially higher than the $(27^{\circ}.5^{+0^{\circ}.8}_{-0^{\circ}.6})$ inclination of the overall binary system (Miller-Jones et al. 2021). However, the inclination constraints on those models can be softened by invoking Comptonization in a mildly-relativistically outflowing corona (Beloborodov 1998; Poutanen et al. 2023). Moreover, Particle In Cell (PIC) and resistive General Relativistic Magnetohydrodynamic (rGRMHD) simulations, in combination with general considerations, reveal an alternative scenario in which the Comptonization is effected by (likely cold) plasmons, generated by magnetic reconnection, plasma turbulence, or both (Beloborodov 2017; Sridhar et al. 2025). In this context, “cold” refers to the fact that the plasma bulk motion (which is mildly relativistic, at most), rather than the random motion of the plasma particles, dominates the photon energization. Alternative models invoke scattering off cold plasma outflows (Begelman & Sikora 1987; Dexter & Begelman 2024) or synchrotron and inverse Compton emission from the jet or jet walls (Moscibrodzka 2024).

With an energy range of ~ 19 –64 keV, the balloon-borne hard X-ray spectropolarimeter *XL-Calibur* complements the 2–8 keV range of *IXPE*. *XL-Calibur* flew on an LDB flight from Esrange, Kiruna, Sweden to near Kugluktuk, Nunavut, Canada for a roughly weeklong flight, observing Cyg X-1 (in its low/hard state) and the Crab Pulsar/Pulsar Wind Nebula. This paper presents

the results from the Cyg X-1 observations. The results from the Crab observations, as well as additional details about the *XL-Calibur* flight and data analysis, can be found in [Awaki et al. \(2025\)](#).

One important advantage of *XL-Calibur* is that the blackbody emission from the inner accretion disk is not thought to significantly contribute to the detected signal in the hard X-ray energy range, whereas such a component may still be sampled within the lower *IXPE* bandpass ([Gierliński & Zdziarski 1999](#)). Furthermore, depending on the model, direct coronal emission and coronal emission reprocessed and reflected off the accretion disk may contribute differently in the $\sim 19\text{--}64\text{ keV}$ band than in the $2\text{--}8\text{ keV}$ band.

Three earlier experiments had reported Cyg X-1 polarization results in the hard X-ray and γ -ray bands. The balloon-borne X-ray polarimetry experiment *PoGO+* measured an upper limit of $<8.6\%$ (at the 90% confidence level) and a point measurement of $(0.0^{+5.6}_{-0.0})\%$ for the $19\text{--}181\text{ keV}$ PD ([Chauvin et al. 2018](#)). At even higher, $>100\text{ keV}$ energies, *AstroSat*, *INTEGRAL*/IBIS, and *INTEGRAL*/SPI observations revealed evidence for polarized emission, likely resulting from the Cyg X-1 jet—the PD they detected is much higher, and the PA is significantly different from those at soft X-ray energies ([Chattopadhyay et al. 2024](#); [Laurent et al. 2011](#); [Jourdain et al. 2012](#); [Rodríguez et al. 2015](#)). The data from *XL-Calibur* thus bridges the gap between the soft X-ray and γ -ray bands with the highest precision polarization measurements of Cyg X-1 in the hard X-rays to date, allowing for an independent constraint on any models invoked to explain the observed emission across the high-energy bandpass.

The rest of the paper is organized in the following manner. We give an overview of the *XL-Calibur* mission and data analysis methods in Section 2. The observations of Cyg X-1 conducted during the 2024 LDB flight are described in Section 3. We then present our Cyg X-1 polarization results in Section 4, before discussing the implications of these results for the origin of the hard X-ray emission, especially in the context of broadband high-energy polarization results, in Section 5.

2. THE *XL-CALIBUR* MISSION

2.1. Telescope design

XL-Calibur ([Abarr et al. 2021](#)) uses a 12m optical bench (truss), composed of carbon-fiber tubes and aluminum joints. The truss supports both the X-ray mirror (almost identical to the mirror onboard *Hitomi* described by [Awaki et al. \(2014\)](#)) on the front end and the rotating scattering polarimeter ([Abarr et al. 2021](#)) enclosed within a $\sim 3.5\text{ cm}$ thick anticon-

cidence $\text{Bi}_4\text{Ge}_3\text{O}_{12}$ (BGO) shield on the rear end ([Iyer et al. 2023](#)). The Wallops Arc Second Pointer (WASP) ([Stuchlik 2017](#); [Galchenko & Pernicka 2022](#)), pointing the telescope towards each astrophysical source of interest, is mounted on the gondola connecting the truss to the balloon. During the 2024 flight, it achieved a pointing precision of $<10\text{ arcsec}$ for $>96\%$ of the observation time.

The X-ray mirror is made of 213 concentric Al shells coated with platinum-carbon multilayers. The mirror achieves a Point Spread Function (PSF) with a half-power diameter of 2 arcmin and an effective area of $\sim 300\text{ cm}^2$ at 20 keV and $\sim 50\text{ cm}^2$ at 60 keV ([Kuramoto et al. 2023](#)).

The scattering polarimeter is composed of an 80 mm long, 12 mm diameter, low-atomic-number beryllium (Be) rod surrounded by sixteen 0.8 mm thick, $20\times 20\text{ mm}^2$ footprint, 64-pixel, high-atomic-number ($Z \sim 50$) Cadmium Zinc Telluride (CZT) detectors. An identical 17^{th} (imaging) CZT detector is positioned behind the scattering rod to capture unscattered X-rays. The entire shield and polarimeter assembly is rotated at a constant speed of ~ 2 revolutions-per-minute throughout the flight, in order to minimize systematic biases due to azimuthal variations of efficiency, threshold, and angular coverage between different pixels.

Photons preferentially scatter in a direction perpendicular to their electric vector position angle (the EVPA, same as the PA) according to the Klein-Nishina distribution, leading to an azimuthal scattering angle distribution of

$$dN/d\psi \propto \frac{N}{2\pi} (1 + p_0 \mu \cos(2(\psi - \psi_0 - \pi/2))),$$

where p_0 is the true PD of the incident beam, ψ_0 is its PA, and μ is the instrument- and observation-specific modulation response (~ 0.43 for *XL-Calibur* observing Cyg X-1 in the hard state) for a 100% linearly-polarized beam ([Aoyagi et al. 2024](#)).¹

The atmospheric absorption of lower-energy photons limits the *XL-Calibur* energy range to photons $\gtrsim 15\text{ keV}$ as measured in the CZTs. We used pixel-dependent energy thresholds to remove lower-energy noise, with the median pixel threshold being $\sim 15.4\text{ keV}$ with a standard deviation of $\sim 4.7\text{ keV}$. The signal flux drops off rapidly at higher energies and goes below the background $\sim 60\text{ keV}$ as measured in the CZTs. Taken together, these effects limit the effective signal energy

¹ As [Awaki et al. \(2025\)](#) describes, the overall modulation factor is likely only known to a (systematic) precision of 0.002. However, this is negligible in comparison with the statistical error/precision that will be stated for the main results of this paper.

range to 15–60 keV as measured in the CZTs after scattering, which corresponds to the range of ~ 19 –64 keV for incident photons, as based on simulations (Aoyagi et al. 2024) wherein physical effects such as Compton scattering and the energy resolution (3.8 keV at 20 keV and 11.7 keV at 64 keV, as detailed in Abarr et al. (2021)) have been accounted for.

2.2. Data analysis

The data analysis uses events that triggered only one CZT pixel and that passed the cuts suppressing noisy channels. Additionally, only events without a BGO shield veto, and of energies between 15 keV and 60 keV as recorded in the CZT detectors, corresponding to ~ 19 –64 keV for the incident photons (see Awaki et al. (2025) for further discussion), are used.

For each event, an azimuthal scattering angle is calculated by assuming that the photon scattered off an offset-corrected scattering location into the CZT channel where it was detected, where the offset used is given by the background-subtracted mean position of counts in the imaging CZT detector for each day (see Aoyagi et al. (2024) for a discussion of the necessity and benefit of such a correction). The azimuthal scattering angle is then converted into the Stokes parameters (Kislat et al. 2015) and referenced to Celestial North by accounting for the rotation of the polarimeter, the bank of the telescope (as calculated by the WASP star trackers and inertial navigation unit), and the 90° angular difference between the preferred scattering direction from the actual PA. We then performed an exposure-weighted background subtraction to obtain the Stokes parameters of the Cyg X-1 signal.

Following the approach in Awaki et al. (2025), initial point-estimates for the PD² and PA are defined by

$$PD = \frac{1}{\mu(I_{on} - I_{off})} \sqrt{(Q_{on} - Q_{off})^2 + (U_{on} - U_{off})^2}$$

$$PA = \frac{1}{2} \arctan \left(\frac{U_{on} - U_{off}}{Q_{on} - Q_{off}} \right).$$

In the case of Cyg X-1, the PD magnitude is comparable to the minimum detectable polarization at 99% confidence level (MDP_{99} , the smallest PD that could be detected at this confidence level), a point at which the bias resulting from the positive-definiteness of the PD will affect the result (Awaki et al. 2025). We thus

² The PD equation is sometimes seen with an extra factor of 2 in the numerator, as in Kislat et al. (2015) and Kiss & Pearce (2024). However, as in the convention used by Kislat & Spooner (2024), we have here absorbed that factor into the definition of the Stokes parameters themselves.

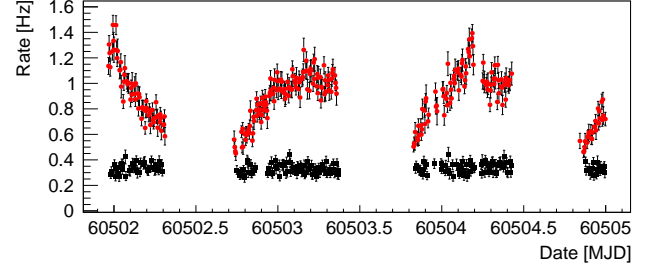


Figure 1. On-source (red circles) and off-source/background (black squares) events, of energies between ~ 19 –64 keV and arriving in the polarimeter detectors, passing the analysis cuts described in Sect. 2.2. Time bins of duration no longer than 300 s are used. The daily gaps between Cyg X-1 observations were used for observing the Crab (Awaki et al. 2025). Smaller variations within each day (for example, the drop in the third observation) are generally correlated with changes in the elevation of the source.

use a Bayesian analysis for determining the probability density distribution of the posterior. A prior of $1/\sqrt{(Q/I)^2 + (U/I)^2}$ is used, which presupposes that all PD and PA values are equally likely (Quinn 2012; Chauvin et al. 2017; Abarr et al. 2020; Kiss & Pearce 2024). Finally, the 1σ error intervals of the PD (positive-definite) and of the PA are found through marginalizing the posterior over the other variable and calculating the values encompassing the densest 68.27% of the total probability. Even in the cases when a measurement is below the MDP_{99} , useful constraints on the PA can still be derived from such Bayesian analyses (Li et al. 2025).

3. THE CYG X-1 OBSERVATIONS AND LIGHTCURVES

XL-Calibur was launched from the Esrange Space Center in Sweden on 2024-07-09 at 03:04 UTC and landed near Kugluktuk in Canada on 2024-07-14 at 23:19 UTC. About forty-three hours were spent observing Cyg X-1 across four days, at elevations between $\sim 25^\circ$ and $\sim 55^\circ$. During these observations, the telescope performed an ON/OFF cross-like nodding pattern centered on the source, with ON observations of 18 minutes each, interspersed with OFF observations (at an offset of 1° from the source) of 12 minutes each.

The rates obtained in the polarimeter during the ON and OFF observations are shown in the lightcurves of Fig. 1, which displays a clear detection of a Cyg X-1 signal rate of up to ~ 1.0 Hz above a stable background rate of ~ 0.35 Hz. The diurnal variations of the signal rate generally stem from the elevation-dependent atmospheric column density, which results in varying levels of detected flux as the source transits the sky each day.

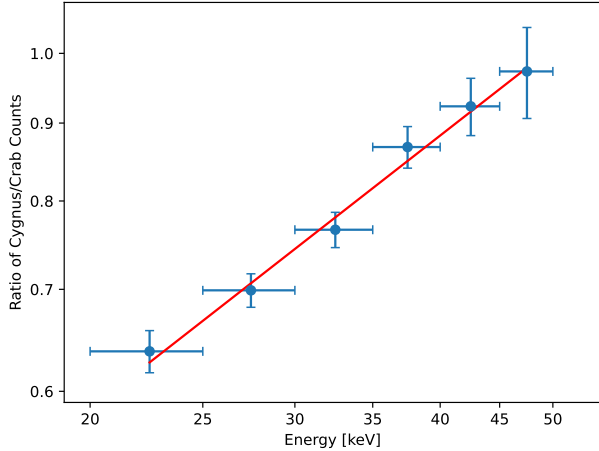


Figure 2. Ratio (blue data points) of the Cyg X-1 to the Crab background-subtracted signal count detection rates as a function of energy, with both axes in logarithmic scale. The counts are between 20 keV to 50 keV, as measured in only the polarimeter CZT detectors, and are binned in intervals of 5 keV. The Cyg X-1 energy spectrum is harder than the Crab spectrum by $\Delta\Gamma \approx 0.60 \pm 0.03$. The red line gives the best linear fit to this ratio spectrum. The uncertainty on the $\Delta\Gamma$ is given by standard error propagation, taking into account the uncertainty arising both from the division of the two spectra as well as from the determination of the linear fit slope.

Across the four days of Cyg X-1 observations, a total number of $\sim 78,500$ events were detected in the sixteen circumjacent (polarimeter) CZT detectors. Out of these 78,500 events, approximately 62,400 arrive during on-source observations of Cyg X-1, and approximately 16,100 occur during off-source observations (purely background events).

Fig. 2 presents the ratio of the Cyg X-1 count-rate spectrum divided by the corresponding Crab spectrum, with both measured by *XL-Calibur* during the same balloon flight with a similar column density distribution (an average line-of-sight column density of 5.5 g/cm^2 for the Crab and 6.0 g/cm^2 for Cyg X-1). This ratio of energy spectra follows a $E^{\Delta\Gamma}$ power law, with $\Delta\Gamma \approx 0.60 \pm 0.03$. The time-averaged energy spectrum of the Crab has a photon index of $\Gamma_{\text{Crab}} = 2.10 \pm 0.02$, as described by Madsen et al. (2015) for the 1–100 keV bandpass (co-spectral with *XL-Calibur*), with $dN/dE \propto E^{-\Gamma_{\text{Crab}}}$.³ Thus, we estimate a Cyg X-1 photon index of

³ We have examined the flux data provided by *SWIFT*/BAT (Krimm et al. 2013), and compared the flux recorded by that instrument (operating in the 15–150 keV range) during the days that *XL-Calibur* observed the Crab, to the flux that it recorded during the time frames coincident with the ones used for the measurements of Madsen et al. (2015). In both cases, the flux is between 0.20 and 0.26 counts/cm²/s.

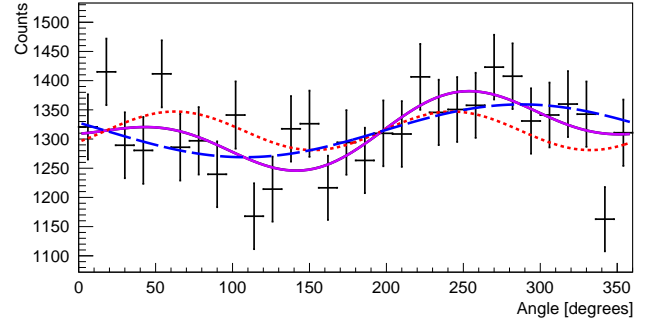


Figure 3. Azimuthal scattering angle distribution (black data points) of the $\sim 19\text{--}64 \text{ keV}$ background-subtracted Cyg X-1 signal arriving in the polarimeter detectors. The overall best-fit (purple solid line) is shown, as well as the 180° component (red dotted line) and 360° component (blue dashed line) contributions to the overall signal.

$\Gamma_{\text{Cyg X-1}} \approx \Gamma_{\text{Crab}} - \Delta\Gamma \approx 1.50 \pm 0.04$ during our observations, consistent with Cyg X-1 being in the hard state (Wilms et al. 2006). A detailed spectral and spectropolarimetric analysis using complete instrument response matrices for *XL-Calibur*, in combination with contemporaneous *NICER* and *NuSTAR* observations, will be published in a forthcoming paper, which will permit a precise determination of the Cyg X-1 spectral index.

4. CYG X-1 HARD X-RAY POLARIMETRIC RESULTS

Fig. 3 displays the background-subtracted azimuthal count distribution, fitted with a component of periodicity 180° as well as a component of periodicity 360° . The former reflects the polarization of the signal; the latter mainly arises from an offset of the telescope’s observing axis from the nominal scattering location at the center of the beryllium rod (Awaki et al. 2025).⁴

The normalized Stokes parameters of the signal are calculated to be $Q/I = 0.033 \pm 0.026$ and $U/I = -0.046 \pm 0.026$. These results for the entire $\sim 19\text{--}64 \text{ keV}$ energy range, as well as results for the $\sim 19\text{--}35 \text{ keV}$ and $\sim 35\text{--}64 \text{ keV}$ energy ranges, are shown in Fig. 4 and listed in Table 1.

Fig. 5 displays the results from the Bayesian analysis, showing the posterior distributions of the PDs and PAs. We infer a marginalized $\sim 19\text{--}64 \text{ keV}$ PD of $(5.0^{+2.7}_{-3.0})\%$ and PA of $-28^\circ \pm 17^\circ$ (Table 1), with uncertainties determined by the 1σ intervals of the marginalized distributions.

⁴ An expected azimuthal variation due to known asymmetries in the mirror PSF will also contribute.

Energy (keV)	Q/I	U/I	PD (%)	PA(°)	MDP_{99} (%)
$\sim 19-64$	0.033 ± 0.026	-0.046 ± 0.026	$5.0^{+2.7}_{-3.0}$	-28 ± 17	7.8
$\sim 19-35$	0.016 ± 0.035	-0.028 ± 0.035	$0.2^{+4.4}_{-0.2}$	-31 ± 40	10.
$\sim 35-64$	0.051 ± 0.038	-0.066 ± 0.038	$7.2^{+4.0}_{-4.4}$	-26 ± 17	12

Table 1. The background-subtracted, normalized Stokes Q and Stokes U results, the marginalised PD and PA values from the Bayesian analysis, and the MDP_{99} values for the *XL-Calibur* observation. The two energy subdivisions are chosen so as to have approximately equal background-subtracted counts. All uncertainties are given at the 1σ level ($\sim 68\%$ Gaussian probability content). The same modulation factor μ is used for all calculations.

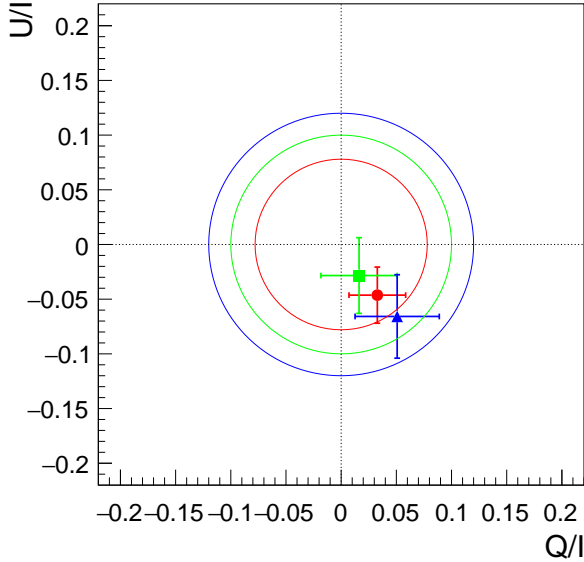


Figure 4. The $\sim 19-64$ keV (red dot), $\sim 19-35$ keV (green square), and $\sim 35-64$ keV (blue triangle) background-subtracted, normalized Stokes results, with errors bars giving the 1σ confidence level. The circles delineate the MDP_{99} values (also given in Table 1) of each of these energy ranges (inner circle $\sim 19-64$ keV, middle circle $\sim 19-35$ keV, and outer circle $\sim 35-64$ keV; all energy ranges as recorded in the CZT detectors).

We derive a concrete measure of statistical significance for the signal by making use of the normalized Stokes parameters, $q = Q/I$ and $u = U/I$, and their 1σ errors, σ_q and σ_u . Using the statistical distance, $d = \sqrt{(q/\sigma_q)^2 + (u/\sigma_u)^2}$, between a polarization measurement and an unpolarized beam, the probability $p_c(d)$ for obtaining a larger PD by chance is given by

$$p_c(d) = \frac{1}{2\pi} \int_d^\infty 2\pi r dr e^{-r^2/2}.$$

For the overall Cyg X-1 result, we thus infer a chance probability of $p_c = 0.087$ for detecting larger PDs than the one we observed, given an unpolarized signal. This measure of significance confirms, more rigorously, the

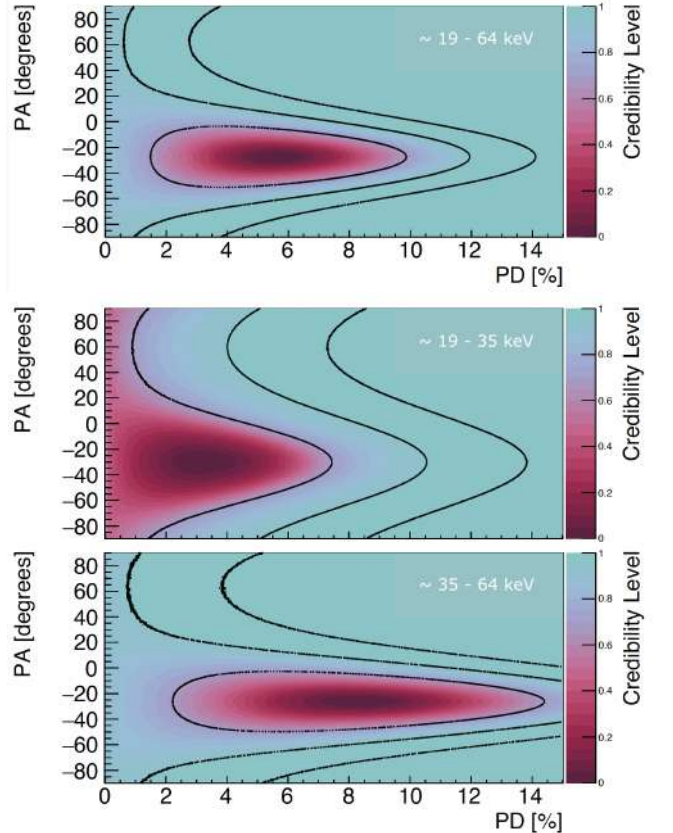


Figure 5. Results from the Bayesian analysis of the *XL-Calibur* data. Contour lines denote the 1σ , 2σ , and 3σ credibility regions. The color/darkness scale denotes the lowest-percentile credibility level into which each region could fall.

approximate significance that one would nominally obtain through dividing the measured PD value in Table 1 by its corresponding error.

5. DISCUSSION AND SUMMARY

XL-Calibur observed Cyg X-1 in the low/hard state in July 2024. The observations revealed a $\sim 19-64$ keV PD of $(5.0^{+2.7}_{-3.0})\%$ at a PA of $-28^\circ \pm 17^\circ$, similar to the $2-8$ keV PD of $(4.01 \pm 0.20)\%$ and PA of $-20^\circ.7 \pm 1^\circ.4$ measured by *IXPE*. The results are also consistent with the previous best measurement, from *PoGO+* (Chauvin et al. 2018), compared to which *XL-Calibur* offers around a factor of two reduction in the PD error. The

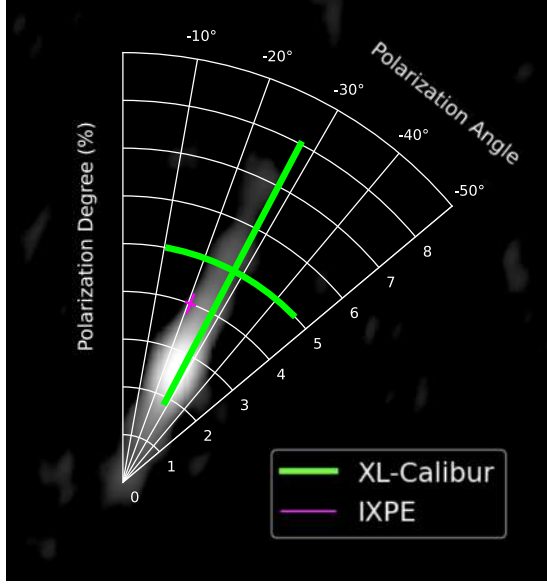


Figure 6. The polar diagram of measured PD and PA values in the X-ray band overlaid atop the radio jet image from VLBA astrometry data (Miller-Jones et al. 2021); PD values are in percent in the radial direction. Results are given for the *XL-Calibur* (green) observation across the entire ~ 19 – 64 keV energy range, as well as for the *IXPE* (magenta) results across its 2 – 8 keV band. The errors bars of the polarization results are given at the 1σ level, as derived from the marginalized Bayesian analysis (for *XL-Calibur*) and as listed in Table S2 of Krawczynski et al. (2022) (for *IXPE*).

measured PA of the hard X-ray emission, just as for the soft X-ray results from *IXPE*, aligns with the radio jet as determined from Very Long Baseline Array (VLBA) observations at 8.4 GHz (Miller-Jones et al. 2021). The overlay of the projection of the polarization results from both bandpasses atop the radio jet image is shown in Fig. 6.

Fig. 7 shows the *XL-Calibur* data in the context of polarization results obtained across the X-ray and γ -ray bands. The low levels of polarization and comparability of the measured PDs and PAs from 2 keV to ~ 64 keV suggest that similar physical mechanisms are responsible for the polarization properties observed in both bands. The ~ 19 – 64 keV X-ray emission from BHXRBS is thought to be dominated by Comptonized emission from the hot coronal plasma, some of which reaches the observer after reflecting at least once off the accretion disk. However, above 100 keV, *AstroSat* and *INTEGRAL* measurements indicate a drastic rise of the PD with respect to energy. Indeed, spectral analyses show that the high-energy emission transitions from being corona-dominated (irrespective of the specific coronal emission model being used to explain the hard X-rays) to being jet-dominated between 100 keV and 1 MeV (see

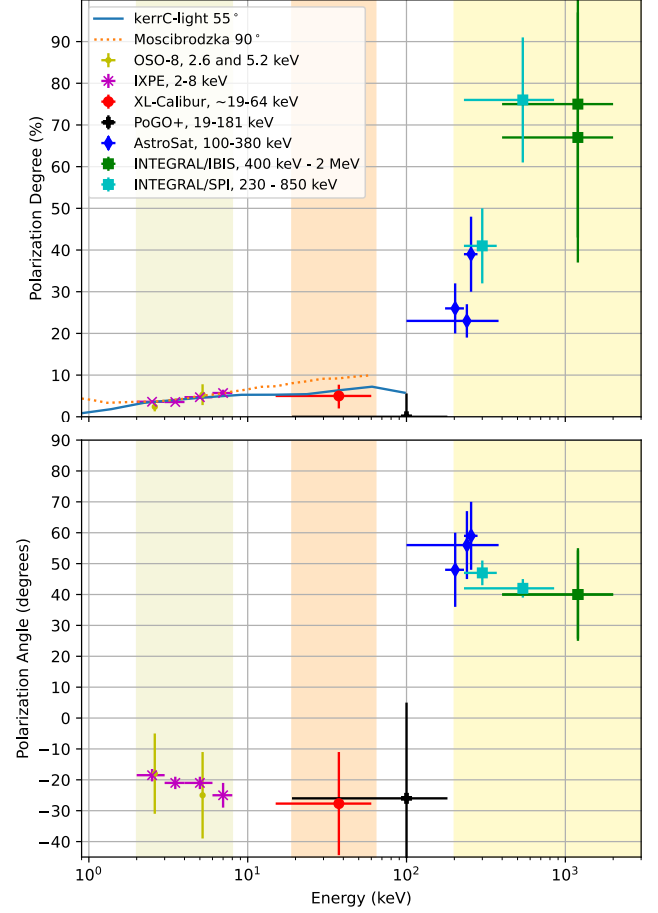


Figure 7. Compilation of Cyg X-1 polarization results from the X-ray band to the gamma-ray band. The shaded regions show the 2 – 8 keV energy range of *IXPE* (left), the ~ 19 – 64 keV energy range of *XL-Calibur* (middle), and the 200 keV– 5 MeV energy range of the upcoming *Compton Spectrometer and Imager (COSI)* (right) (Tomsick et al. 2024). The multiwavelength data are taken from Long et al. (1980); Krawczynski et al. (2022); Chauvin et al. (2018); Chattopadhyay et al. (2024); Laurent et al. (2011); Jourdain et al. (2012); Rodriguez et al. (2015). All of these measurements observe Cyg X-1 in some hard (or intermediate-hard) state (Chattopadhyay et al. 2024), except for *OSO-8*. The solid blue line delineates the PD prediction of the 55° inclination *kerrC-light* model (see text; see also Krawczynski & Beheshtipour (2022)). The dotted orange line delineates the PD prediction of the 90° model from Moscibrodzka (2024). Both of these models predict a slight increase of the PD and a roughly constant PA, parallel to the jet, across the *IXPE* and *XL-Calibur* energy ranges.

Kantzas et al. 2021, and references therein). Moreover, the PA seems to swing by $\sim 90^\circ$ between the *XL-Calibur* and *AstroSat* energy ranges, as would be expected for a transition from emission Comptonized in a horizontally-extended corona to synchrotron and/or inverse Compton emission from a jet with an axial magnetic field.

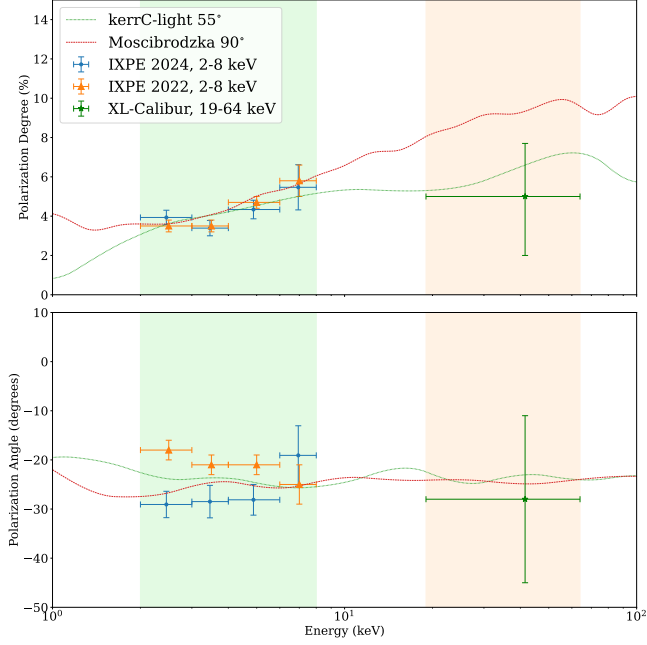


Figure 8. A zoom-in on the models and data in the X-ray band. The *kerrC* model is a Monte Carlo-based model: 68,040 combinations of system parameters were simulated, with 20,000,000 photons used for each configuration. The *IXPE* 2024 data come from *IXPE* observations 03010001, 03010101, and 03003101 of Cyg X-1, which were taken within a couple months before the *XL-Calibur* observation, and are analyzed jointly with *ixpeobssim* (Baldini et al. 2022).

However, the *AstroSat* and *INTEGRAL* results were obtained from instruments not specifically built for polarimetry, leading to larger systematic errors on the results. The *COSI* mission, a large and uniform Compton telescope for polarimetry to be launched in 2027, should help resolve this question with precise polarization measurements in its energy range of 200 keV – 5 MeV (Tom-sick et al. 2022).

Focusing in on the X-ray band: Figs. 7 and 8 compare the *IXPE*, *PoGO+*, and *XL-Calibur* results with various published theoretical estimates. The prediction of the *kerrC*-light model (Krawczynski & Beheshtipour 2022), given by the solid line in Fig. 7, assumes a wedge-shaped corona sandwiching a thin, 100%-reflecting accretion disk. The reflection is modeled using Chandrasekhar’s classical results for an infinitely deep electron scattering atmosphere (Chandrasekhar 1960). This model has the same parameter values as shown in Table S3 of Krawczynski et al. (2022), save for a dimensionless spin parameter a ($-1 \leq a \leq 1$) of 0.94 (as measured by Walton et al. (2016)), an increased accretion rate (for flux normalization purposes), and an inclination angle of 55° (the angle that best fits both soft and hard X-ray data, as shown in Fig. 9, given these parameters). Such

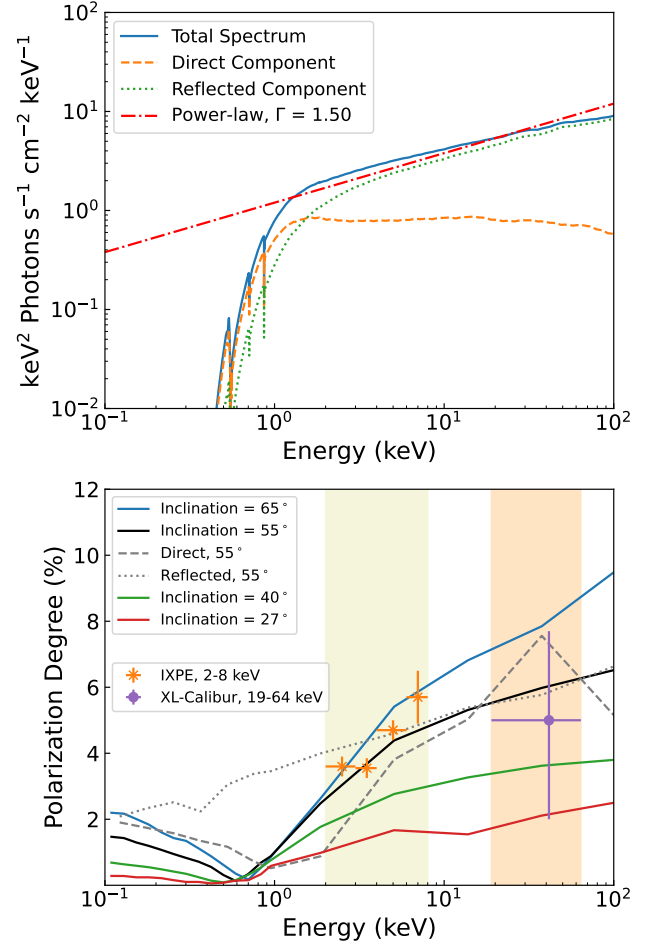


Figure 9. Top: Simulated Cyg X-1 energy spectrum from the *kerrC*-light code, assuming a geometrically thin, optically thick accretion disk with a sandwich corona of opening angle 10° , of optical depth $\tau = 0.41$, and of inclination angle 55° . While the dashed orange line shows the flux of the photons that reach the observer without any scattering off the disk, the dotted green line shows the flux of the photons scattering off the disk one or several times. A dotted-dashed red line is also presented to indicate the power-law index calculated in Fig. 2. Bottom: Polarization degree spectra of the *kerrC*-light model from the above panel, varying only the inclination in each instance (with the model from the highest inclination having the highest PDs). The *IXPE* (from 2022) and *XL-Calibur* data are overlaid, as in Figs. 7 and 8. PD as a function of energy, for the direct and reflected components, is also plotted for the 55° case as dashed and dotted grey lines. The abrupt changes in the flux of the direct component at higher energies reflects the low statistics due to the low proportion of flux it comprises at those energies.

a model predicts a slight increase of PD (from $\sim 2\%$ to $\sim 6\%$) when going from soft to hard X-rays, as well as a stable PA, parallel to the black hole spin axis. This model is thus one model that is consistent with both the *IXPE* and *XL-Calibur* results.

The top panel of Fig. 9 offers a closer look at this model of inclination 55° , showing the total predicted energy spectrum, as well as the spectrum subdivided into ‘direct’ and ‘reflected’ contributions. The accretion disk emits photons of about a few keV in energy, and these photons gain more energy the more often they scatter in the corona. For a sandwich corona, a larger number of scatterings for a photon (that is, a photon more likely to be at a higher energy) is accompanied by a higher likelihood of one or more encounters and reflections off the disk, given the geometry. In the sandwich model, reflection off the disk thus becomes an integral part of the Comptonization process, and the fraction of reflected photons increases with increasing photon energy. The distinction between direct coronal emission and reflected coronal emission is thus not as meaningful as it would be for models using a more localized corona situated further away from the disk. The power-law index of 1.55 calculated in Fig. 2 is overplotted in Fig. 7, displaying a reasonable agreement with the spectral flux predicted by *kerrC*-light in the X-ray regime.

As a further examination of the inclination angles, the bottom panel of Fig. 9 shows the PDs predicted by *kerrC*-light models at several possible inclinations of the black hole. The PDs of the direct and reflected components of the $i = 55^\circ$ model are plotted, as mentioned above, as well. As expected, the PD of the overall model starts very closely following the PD of the reflected component at about the same energy that the reflected flux becomes dominant in the top panel. Models with inclinations $< 40^\circ$ have difficulty explaining both the observed *IXPE* and *XL-Calibur* PDs. For example, for an inclination of $i = 27^\circ$, which is close to the inferred inclination angle of the binary (Miller-Jones et al. 2021) the sandwich model of *kerrC*-light maintains a PD below 3% through the end of the *XL-Calibur* range. However, Beloborodov (1998); Poutanen et al. (2023) emphasize that higher PDs can result from coronal plasma outflowing at $\sim 40\%$ the speed of light or faster, thus allowing for lower inclination angles.

As mentioned in the introduction, several alternative, but related, models have also been proposed in the literature. In the model of Moscibrodzka (2024), the X-rays come from the inverse Compton scattering of Bremsstrahlung and synchrotron emission produced in the outflowing jet wall. The high-inclination (90°) result from their General Relativistic *Radiative* Magnetohydrodynamic simulations reproduces the observed alignment of the soft and hard X-ray PAs with the radio jet, as well as generally tracking the change in PD between the lower and higher energy bands (as displayed in Figs. 7 and 8). Similarly, Dexter & Begelman (2024)

argue that the Cyg X-1 PDs and PAs can be explained by the inverse Compton scattering of disk emission by a mildly-relativistic ($\sim 75\%$ of the speed of light) cold outflow in the shape of a hollow cone, centered on the black hole spin axis, into which the observer looks. Sridhar et al. (2025), using General Relativistic *Resistive* Magnetohydrodynamic simulations, give a physical scenario which could lead to such a configuration: magnetic reconnection producing cold plasmoids, with bulk motion, that inverse Compton scatter longer-wavelength photons into the *IXPE* and *XL-Calibur* energy bands. All of these models predict little variation of the PD and PA, provided that the *IXPE* signal is not heavily contaminated by disk emission.

Although the present data starts to provide some indication, a final decision between models of hard X-ray emission from BHXRBs will require both (i) additional observations of BHXRBs in the hard and soft states with the best possible broadband (measuring both soft and hard X-rays) spectropolarimetric coverage, as well as (ii) continued refinement of the various theoretical models. Future flights of *XL-Calibur* will contribute to this goal through constraining the polarization from more BHXRBs in the hard X-rays. A longer flight from McMurdo in Antarctica, observing southern-hemisphere sources, such as GX 339-4, 4U 1630-47, Swift J1727.8-1613, LMC X-1, and LMC X-3, will significantly increase the number of BHXRBs studied in this energy range, as well as the precision of their polarization measurements.

ACKNOWLEDGMENTS

XL-Calibur is a joint mission supported by NASA, JAXA, and the Swedish National Space Agency *Rymdstyrelsen*. We sincerely thank James Miller-Jones for the data used to produce the VLBA radio jet image. We acknowledge NASA support under grant 80NSSC24K0205. KTH authors are supported by the Swedish National Space Agency (2022-00178 and 2024-00248). MP also acknowledges funding from the Swedish Research Council *Vetenskapsrådet* (2021-05128). The Washington University in St. Louis group acknowledges additional NASA support through the grants 80NSSC20K0329, 80NSSC21K1817, 80NSSC22K1291, 80NSSC22K1883, 80NSSC23K1041, and 80NSSC24K1178, as well as funding from the McDonnell Center for the Space Sciences at Washington University in St. Louis. The University of New Hampshire group acknowledges additional NASA support through the grants 80NSSC24K0636 and 80NSSC24K1762. The Japanese Society for the Promotion of Science (JSPS) has supported this

work through KAKENHI Grant Numbers 19H01908, 19H05609, 20H00175 (HM), 20H00178 (HM), 21K13946 (YU), 22H01277 (YM), 23H00117, and 23H00128 (HM).

DATA AVAILABILITY

The XL-Calibur data underlying this article will be made available via the NASA HEASARC data archive, at <https://heasarc.gsfc.nasa.gov/docs/xlcalibur/>.

REFERENCES

- Abarr, Q., Baring, M., Beheshtipour, B., et al. 2020, *ApJ*, 891, 70, doi: [10.3847/1538-4357/ab672c](https://doi.org/10.3847/1538-4357/ab672c)
- Abarr, Q., Awaki, H., Baring, M. G., et al. 2021, *Astroparticle Physics*, 126, 102529, doi: [10.1016/j.astropartphys.2020.102529](https://doi.org/10.1016/j.astropartphys.2020.102529)
- Aoyagi, M., Bose, R. G., Chun, S., et al. 2024, *Astroparticle Physics*, 158, 102944, doi: [10.1016/j.astropartphys.2024.102944](https://doi.org/10.1016/j.astropartphys.2024.102944)
- Awaki, H., Kunieda, H., Ishida, M., et al. 2014, *ApOpt*, 53, 7664, doi: [10.1364/AO.53.007664](https://doi.org/10.1364/AO.53.007664)
- Awaki, H., Baring, M. G., Bose, R., et al. 2025, *MNRAS*, doi: [10.1093/mnras/1516026](https://doi.org/10.1093/mnras/1516026)
- Baldini, L., Bucciantini, N., Lalla, N. D., et al. 2022, *SoftwareX*, 19, 101194, doi: [10.1016/j.softx.2022.101194](https://doi.org/10.1016/j.softx.2022.101194)
- Begelman, M. C., & Sikora, M. 1987, *ApJ*, 322, 650, doi: [10.1086/165760](https://doi.org/10.1086/165760)
- Beloborodov, A. M. 1998, *The Astrophysical Journal*, 510, L123, doi: [10.1086/311810](https://doi.org/10.1086/311810)
- Beloborodov, A. M. 2017, *ApJ*, 850, 141, doi: [10.3847/1538-4357/aa8f4f](https://doi.org/10.3847/1538-4357/aa8f4f)
- Cavero, N. R., & IXPE Collaboration. 2024, in *Multifrequency Behaviour of High Energy Cosmic Sources XIV*, 39
- Chandrasekhar, S. 1960, *Radiative transfer*
- Chattopadhyay, T., Kumar, A., Rao, A. R., et al. 2024, *ApJL*, 960, L2, doi: [10.3847/2041-8213/ad118d](https://doi.org/10.3847/2041-8213/ad118d)
- Chauvin, M., Florén, H. G., Friis, M., et al. 2017, *Scientific Reports*, 7, 7816, doi: [10.1038/s41598-017-07390-7](https://doi.org/10.1038/s41598-017-07390-7)
- . 2018, *Nature Astronomy*, 2, 652, doi: [10.1038/s41550-018-0489-x](https://doi.org/10.1038/s41550-018-0489-x)
- Dexter, J., & Begelman, M. C. 2024, *MNRAS*, 528, L157, doi: [10.1093/mnras/sl4d182](https://doi.org/10.1093/mnras/sl4d182)
- Doroshenko, V., Poutanen, J., Tsygankov, S. S., et al. 2022, *Nature Astronomy*, 6, 1433, doi: [10.1038/s41550-022-01799-5](https://doi.org/10.1038/s41550-022-01799-5)
- Dovčiak, M., Podgorný, J., Svoboda, J., et al. 2024, *Galaxies*, 12, 54, doi: [10.3390/galaxies12050054](https://doi.org/10.3390/galaxies12050054)
- Ehlert, S. R., Ferrazzoli, R., Marinucci, A., et al. 2022, *ApJ*, 935, 116, doi: [10.3847/1538-4357/ac8056](https://doi.org/10.3847/1538-4357/ac8056)
- Galchenko, P., & Pernicka, H. 2022, *Journal of Guidance Control Dynamics*, 45, 1365, doi: [10.2514/1.G006465](https://doi.org/10.2514/1.G006465)
- Gianolli, V. E., Kim, D. E., Bianchi, S., et al. 2023, *MNRAS*, 523, 4468, doi: [10.1093/mnras/stad1697](https://doi.org/10.1093/mnras/stad1697)
- Gianolli, V. E., Bianchi, S., Kammoun, E., et al. 2024, *A&A*, 691, A29, doi: [10.1051/0004-6361/202451645](https://doi.org/10.1051/0004-6361/202451645)
- Gierliński, M., & Zdziarski, A. A. 1999, in *Astronomical Society of the Pacific Conference Series*, Vol. 161, *High Energy Processes in Accreting Black Holes*, ed. J. Poutanen & R. Svensson, 64, doi: [10.48550/arXiv.astro-ph/9811220](https://doi.org/10.48550/arXiv.astro-ph/9811220)
- Grinberg, V., Hell, N., Pottschmidt, K., et al. 2013, *A&A*, 554, A88, doi: [10.1051/0004-6361/201321128](https://doi.org/10.1051/0004-6361/201321128)
- Ingram, A., Ewing, M., Marinucci, A., et al. 2023, *MNRAS*, 525, 5437, doi: [10.1093/mnras/stad2625](https://doi.org/10.1093/mnras/stad2625)
- Ingram, A., Bollemeijer, N., Veledina, A., et al. 2024, *ApJ*, 968, 76, doi: [10.3847/1538-4357/ad3faf](https://doi.org/10.3847/1538-4357/ad3faf)
- Iyer, N. K., Kiss, M., Pearce, M., et al. 2023, *Nuclear Instruments and Methods in Physics Research A*, 1048, 167975, doi: [10.1016/j.nima.2022.167975](https://doi.org/10.1016/j.nima.2022.167975)
- Johnston, K. J., Elvis, M., Kjer, D., & Shen, B. S. P. 1982, *ApJ*, 262, 61, doi: [10.1086/160396](https://doi.org/10.1086/160396)
- Jourdain, E., Roques, J. P., Chauvin, M., & Clark, D. J. 2012, *ApJ*, 761, 27, doi: [10.1088/0004-637X/761/1/27](https://doi.org/10.1088/0004-637X/761/1/27)
- Kantzas, D., Markoff, S., Beuchert, T., et al. 2021, *MNRAS*, 500, 2112, doi: [10.1093/mnras/staa3349](https://doi.org/10.1093/mnras/staa3349)
- Kislat, F., Clark, B., Beilicke, M., & Krawczynski, H. 2015, *Astroparticle Physics*, 68, 45, doi: [10.1016/j.astropartphys.2015.02.007](https://doi.org/10.1016/j.astropartphys.2015.02.007)
- Kislat, F., & Spooner, S. 2024, in *Handbook of X-ray and Gamma-ray Astrophysics*, ed. C. Bambi & A. Santangelo (Singapore: Springer Nature Singapore), 5853, doi: [10.1007/978-981-16-4544-0_141-1](https://doi.org/10.1007/978-981-16-4544-0_141-1)
- Kiss, M., & Pearce, M. 2024, in *Handbook of X-ray and Gamma-ray Astrophysics*, ed. C. Bambi & A. Santangelo (Singapore: Springer Nature Singapore), 5683, doi: [10.1007/978-981-16-4544-0_141-1](https://doi.org/10.1007/978-981-16-4544-0_141-1)
- Krawczynski, H., & Beheshtipour, B. 2022, *ApJ*, 934, 4, doi: [10.3847/1538-4357/ac7725](https://doi.org/10.3847/1538-4357/ac7725)
- Krawczynski, H., Muleri, F., Dovčiak, M., et al. 2022, *Science*, 378, 650, doi: [10.1126/science.add5399](https://doi.org/10.1126/science.add5399)
- Krimm, H. A., Holland, S. T., Corbet, R. H. D., et al. 2013, *ApJS*, 209, 14, doi: [10.1088/0067-0049/209/1/14](https://doi.org/10.1088/0067-0049/209/1/14)

- Kuramoto, H., Matsumoto, H., Awaki, H., et al. 2023, in Society of Photo-Optical Instrumentation Engineers (SPIE) Conference Series, Vol. 12679, Optics for EUV, X-Ray, and Gamma-Ray Astronomy XI, ed. S. L. O'Dell, J. A. Gaskin, G. Pareschi, & D. Spiga, 126791B, doi: [10.1117/12.2676572](https://doi.org/10.1117/12.2676572)
- Laurent, P., Rodriguez, J., Wilms, J., et al. 2011, *Science*, 332, 438, doi: [10.1126/science.1200848](https://doi.org/10.1126/science.1200848)
- Li, H., Zhao, Q.-C., Feng, H., Tao, L., & Tsygankov, S. S. 2025, arXiv e-prints, arXiv:2504.04775, doi: [10.48550/arXiv.2504.04775](https://doi.org/10.48550/arXiv.2504.04775)
- Li, L.-X., Narayan, R., & McClintock, J. E. 2009, *ApJ*, 691, 847, doi: [10.1088/0004-637X/691/1/847](https://doi.org/10.1088/0004-637X/691/1/847)
- Liodakis, I., Marscher, A. P., Agudo, I., et al. 2022, *Nature*, 611, 677, doi: [10.1038/s41586-022-05338-0](https://doi.org/10.1038/s41586-022-05338-0)
- Long, K. S., Chanan, G. A., & Novick, R. 1980, *ApJ*, 238, 710, doi: [10.1086/158027](https://doi.org/10.1086/158027)
- Madsen, K. K., Reynolds, S., Harrison, F., et al. 2015, *ApJ*, 801, 66, doi: [10.1088/0004-637X/801/1/66](https://doi.org/10.1088/0004-637X/801/1/66)
- Mastroserio, G., De Marco, B., Baglio, M. C., et al. 2024, arXiv e-prints, arXiv:2408.06856, doi: [10.48550/arXiv.2408.06856](https://doi.org/10.48550/arXiv.2408.06856)
- Miller-Jones, J. C. A., Bahramian, A., Orosz, J. A., et al. 2021, *Science*, 371, 1046, doi: [10.1126/science.abb3363](https://doi.org/10.1126/science.abb3363)
- Moscibrodzka, M. 2024, *Ap&SS*, 369, 68, doi: [10.1007/s10509-024-04333-3](https://doi.org/10.1007/s10509-024-04333-3)
- Poutanen, J., Veledina, A., & Beloborodov, A. M. 2023, *ApJL*, 949, L10, doi: [10.3847/2041-8213/acd33e](https://doi.org/10.3847/2041-8213/acd33e)
- Poutanen, J., & Vilhu, O. 1993, *A&A*, 275, 337
- Quinn, J. L. 2012, *A&A*, 538, A65, doi: [10.1051/0004-6361/201015785](https://doi.org/10.1051/0004-6361/201015785)
- Rodriguez, J., Grinberg, V., Laurent, P., et al. 2015, *ApJ*, 807, 17, doi: [10.1088/0004-637X/807/1/17](https://doi.org/10.1088/0004-637X/807/1/17)
- Saade, M. L., Kaaret, P., Liodakis, I., & Ehlert, S. R. 2024, *ApJ*, 974, 101, doi: [10.3847/1538-4357/ad73a3](https://doi.org/10.3847/1538-4357/ad73a3)
- Schnittman, J. D., & Krolik, J. H. 2009, *ApJ*, 701, 1175, doi: [10.1088/0004-637X/701/2/1175](https://doi.org/10.1088/0004-637X/701/2/1175)
- . 2010, *ApJ*, 712, 908, doi: [10.1088/0004-637X/712/2/908](https://doi.org/10.1088/0004-637X/712/2/908)
- Sridhar, N., Ripperda, B., Sironi, L., Davelaar, J., & Beloborodov, A. M. 2025, *ApJ*, 979, 199, doi: [10.3847/1538-4357/ada385](https://doi.org/10.3847/1538-4357/ada385)
- Steiner, J. F., Nathan, E., Hu, K., et al. 2024, *ApJL*, 969, L30, doi: [10.3847/2041-8213/ad58e4](https://doi.org/10.3847/2041-8213/ad58e4)
- Stuchlik, D. 2017, The NASA Wallops Arc-Second Pointer (WASP) System for Precision Pointing of Scientific Balloon Instruments and Telescopes, doi: [10.2514/6.2017-3609](https://doi.org/10.2514/6.2017-3609)
- Sunyaev, R. A., & Titarchuk, L. G. 1985, *A&A*, 143, 374
- Taverna, R., Turolla, R., Muleri, F., et al. 2022, *Science*, 378, 646, doi: [10.1126/science.add0080](https://doi.org/10.1126/science.add0080)
- Tomsick, J., Boggs, S., Zoglauer, A., et al. 2024, in 38th International Cosmic Ray Conference, 745, doi: [10.48550/arXiv.2308.12362](https://doi.org/10.48550/arXiv.2308.12362)
- Tomsick, J. A., Lowell, A., Lazar, H., Sleator, C., & Zoglauer, A. 2022, in Handbook of X-ray and Gamma-ray Astrophysics, ed. C. Bambi & A. Sanganello, 73, doi: [10.1007/978-981-16-4544-0_145-1](https://doi.org/10.1007/978-981-16-4544-0_145-1)
- Ulvstad, J. S., Roy, A. L., Colbert, E. J. M., & Wilson, A. S. 1998, *ApJ*, 496, 196, doi: [10.1086/305382](https://doi.org/10.1086/305382)
- Unger, S. W., Lawrence, A., Wilson, A. S., Elvis, M., & Wright, A. E. 1987, *MNRAS*, 228, 521, doi: [10.1093/mnras/228.3.521](https://doi.org/10.1093/mnras/228.3.521)
- Veledina, A., Muleri, F., Dovčiak, M., et al. 2023, *ApJL*, 958, L16, doi: [10.3847/2041-8213/ad0781](https://doi.org/10.3847/2041-8213/ad0781)
- Vink, J., Prokhorov, D., Ferrazzoli, R., et al. 2022, *ApJ*, 938, 40, doi: [10.3847/1538-4357/ac8b7b](https://doi.org/10.3847/1538-4357/ac8b7b)
- Walton, D. J., Tomsick, J. A., Madsen, K. K., et al. 2016, *ApJ*, 826, 87, doi: [10.3847/0004-637X/826/1/87](https://doi.org/10.3847/0004-637X/826/1/87)
- Weisskopf, M. C., Soffitta, P., Baldini, L., et al. 2022, *Journal of Astronomical Telescopes, Instruments, and Systems*, 8, 026002, doi: [10.1117/1.JATIS.8.2.026002](https://doi.org/10.1117/1.JATIS.8.2.026002)
- Wilms, J., Nowak, M. A., Pottschmidt, K., Pooley, G. G., & Fritz, S. 2006, *A&A*, 447, 245, doi: [10.1051/0004-6361:20053938](https://doi.org/10.1051/0004-6361:20053938)
- Wood, C. M., Miller-Jones, J. C. A., Bahramian, A., et al. 2024, *ApJL*, 971, L9, doi: [10.3847/2041-8213/ad6572](https://doi.org/10.3847/2041-8213/ad6572)
- Xie, F., Di Marco, A., La Monaca, F., et al. 2022, *Nature*, 612, 658, doi: [10.1038/s41586-022-05476-5](https://doi.org/10.1038/s41586-022-05476-5)
- Zhang, W., Dovčiak, M., & Bursa, M. 2019, *ApJ*, 875, 148, doi: [10.3847/1538-4357/ab1261](https://doi.org/10.3847/1538-4357/ab1261)